Toward an Autonomous Robotic Battery Materials Research Platform Powered by Automated Workflow and Ontologized Findable, Accessible, Interoperable, and Reusable Data Management

Enea Svaluto-Ferro, Graham Kimbell, YeonJu Kim, Nukorn Plainpan, Benjamin Kunz, Lina Scholz, Raphael Läubli, Maximilian Becker, David Reber, Peter Kraus, Ruben-Simon Kühnel, and Corsin Battaglia*

The discovery of novel battery materials has been accelerated by advanced modeling and machine learning. However, their integration into battery cells remains constrained by the necessity for experimental validation. The status of development and validation of the automated robotic battery materials research platform Aurora is presented, enabling rapid testing of scientific hypotheses and validation of physical models. Aurora integrates electrolyte formulation, battery cell assembly, and battery cell cycling into a stepwise automated application-relevant workflow. The different features of the Aurora platform can be leveraged to design experiments elucidating the impact of cycling parameters, electrode composition, and balancing, and electrolyte formulation on battery performance and long-term cycling stability with the example of NMC∥graphite and LFP∥graphite cells with carbonate-based electrolytes, which serve as benchmark battery cell chemistries. A large, structured, dataset with ontologized metadata detailing cell assembly and cycling protocols, alongside corresponding time series cycling data for all cells is provided as open research data. This study establishes Aurora as a powerful research platform for accelerating battery materials research.

1. Introduction

The development of advanced materials has been a major driving force behind technological innovation and plays a critical role in addressing global societal challenges. Breakthroughs in materials science are needed to combat climate change by enabling cleaner batteries, more efficient carbon capture, and better catalysts to convert carbon back into fuels, chemicals, and other value-added products. Despite significant progress in predicting new materials with tailored functional properties using advanced materials modeling and machine learning, the rate of discovery remains constrained by the often time-consuming and resource-intensive experimental realization and validation of new materials.

To accelerate the pace of materials discovery and overcome the bottleneck of experimental validation, automated high-throughput experimentation has emerged as a necessity.[1–4] While the pharmaceutical industry has long embraced such methods for drug discovery,[5] their application to energy materials is still in its early stages, with much potential yet to be realized in this field.[6,7] By integrating high-throughput experimentation with artificial intelligence, a closed loop can be established, in which experimental data is fed back into machine learning models to refine predictions, optimize materials combinations, and guide further experimentation, thereby accelerating the discovery process and reducing the reliance on trial-and-error.

These observations also hold for the discovery of new battery chemistries, where the challenge extends beyond identifying individual materials to finding combinations of materials that interact synergistically.[8–12] High-throughput experimentation allows for rapid screening, enabling the identification of optimal battery materials combinations and battery cycling parameters that optimize key performance metrics such as energy and power density, cycling stability, as well as cost and sustainability targets.

Besides reports on systems that automate the synthesis and characterization of novel battery electrode and electrolyte

E. Svaluto-Ferro, G. Kimbell, Y. J. Kim, N. Plainpan, B. Kunz, L. Scholz, R. Läubli, M. Becker, D. Reber, P. Kraus, R.-S. Kühnel, C. Battaglia
Empa - Swiss Federal Laboratories for Materials Science and Technology
Ueberlandstrasse 129, Dübendorf 8600, Switzerland
E-mail: corsin.battaglia@empa.ch

L. Scholz, R. Läubli, C. Battaglia
Department of Information Technology and Electrical Engineering
ETH Zurich
Gloriastrasse 35, Zurich 8092, Switzerland

C. Battaglia
School of Engineering
Institute of Materials
EPFL
Station 15, Lausanne 1015, Switzerland

C. Battaglia
Tandon School of Engineering
Chemical and Biomolecular Engineering
NYU
6 MetroTech Center, Brooklyn, NY 11201, USA

Supporting information for this article is available on the WWW under https://doi.org/10.1002/batt.202500155

materials,[13–24] only a few reports discuss the automated integration and characterization of novel materials directly into battery cells.[25–27] Most of these robotic platforms assemble coin cell batteries, which remain the cornerstone for early-stage battery materials evaluation.[28–32] However, automated cell assembly in inert atmosphere remains a formidable challenge due to the complexity of handling the different cell components requiring different handling tools and frequent tool changes, the limited accessibility and confined workspace inside the glovebox complicating robot maintenance and calibration, the strict requirement to prevent ambient air intrusion and minimize outgassing from robotic components, etc.

As robotic cell assembly platforms described in earlier reports overcome initial challenges, mature, and become available commercially, there is a corresponding improvement in cell yield and data quality. However, the integration of robotics into the design of experiments requires rigorous validation to ensure consistency and reliability. This study presents a comprehensive validation of our automated battery research platform, called Aurora, highlighting its key features and capabilities in the context of automated battery experimentation.

2. Experimental Section

The Aurora platform is capable of automating 1) battery electrolyte formulation, 2) coin cell assembly, and 3) cell cycling. The first two steps are accomplished by a dedicated automated workflow implemented onto a standardized robotic platform (Chemspeed Technologies SwingXL), which was adapted for this purpose and integrated into an argon-filled glovebox (MBraun). Snapshots illustrating different stages of the cell assembly workflow on the Aurora cell assembly platform are shown in **Figure 1**. A video of the cell assembly process is available as Supporting Information.

The platform is equipped with a four-axes robotic arm (displacement in each of three directions in steps of $0.10 \, \text{mm} \pm 0.01 \, \text{mm}$, rotation around the vertical axis in steps of $0.05° \pm 0.01°$) that has access to a number of interchangeable tools to manipulate the different coin cell components including the electrolyte.

On the very left of Figure 1a is the electrolyte mixing station. While dedicated powder dosing units are available for dosing, e.g., electrolyte salts or electrolyte additives, electrolyte components are currently supplied as preprepared concentrated stock solutions in larger vials (20 mL), which are then mixed into diluted individual electrolyte formulations in smaller vials (8 mL) employing either volumetric or gravimetric liquid dispensing.

Coin cell components including the negative and positive electrode and the separator are supplied on aluminum microteter plates containing an array of wells visible in the middle of Figure 1a, into which the components are placed manually before automated weighing and assembly. The wells have dedicated diameters for each component and a conical shape to center the components. We are currently operating the platform with R2032 coin cell format components with 15 mm diameter negative electrodes, 14 mm diameter positive electrodes, and 16 mm diameter separators. These dimensions could be changed by
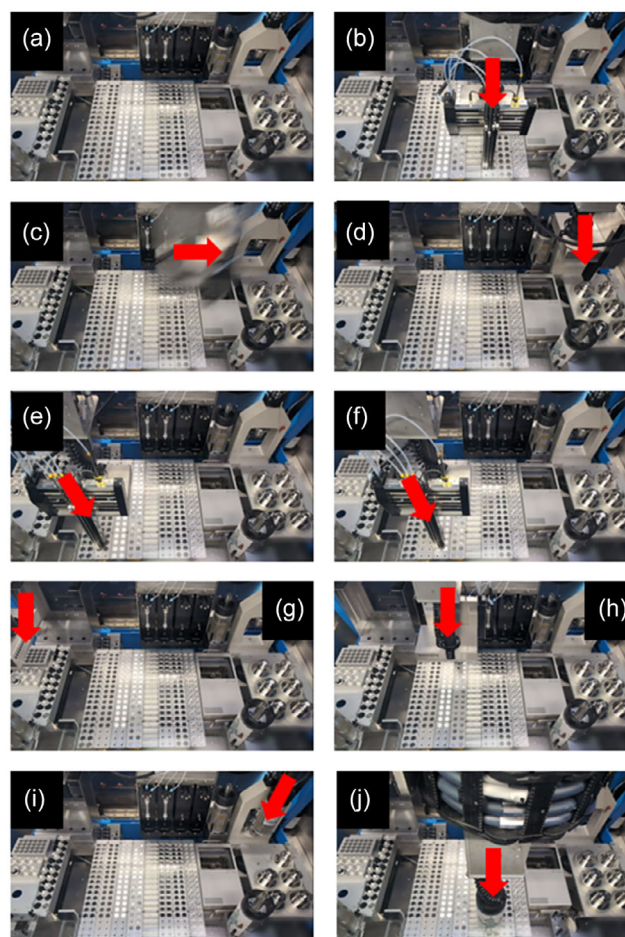

Figure 1. Aurora's coin cell assembly platform at different stages of the cell assembly process: a) all cell components supplied on microtiter plates and ready to go, b) pick-up of cell can, c) transfer to crimping die, d) release of cell can on crimping die, e) pick-up of negative electrode, f) pick-up of separator, g) aspiration of electrolyte, h) pick-up of positive electrode, i) crimping of coin cell stack in crimping station, and j) release of assembled coin cell on microtiter plate. The red arrows indicate the position of the robot arm. See also the video of Aurora in action in the Supporting Information.

exchanging the aluminum microteter plates. An automated dispensing system for stock coin cell components (cell can, cell lid, seal, spacer, and spring) is currently under construction and will replace approximately half of these plates in the near future, freeing space on the platform to build more cells per batch or implement additional features. The current platform layout allows the assembly of up to 36 coin cells per batch.

Before assembly, electrodes are automatically weighed on a dedicated balance and the weight for each electrode is recorded. This is a very useful feature to balance the areal capacities of available positive and negative electrodes in pairs according to predefined rules. Coin cells are then assembled on one of the six crimping dies and sealed on the crimping station, depicted on the very right of Figure 1a. A single crimping die would in principle be sufficient to assemble all 36 coin cells sequentially. To reduce the time required for tool changes, we use multiple dies, such that cells can be assembled and crimped in parallel in groups of six. The assembly sequence can be configured for

each run individually. A video camera mounted inside the glovebox is monitoring the assembly of the cells on the dies. The camera enables us to monitor the progress and quantify component misalignment within cells. We plan on adding active feedback from the camera, e.g., auto alignment of components and detection of assembly issues in the near future.

After cell assembly, cells are transferred to a dedicated coin cell cycling platform consisting of 256 potentiostat channels with electrochemical impedance spectroscopy capability (BioLogic MPG-2) routed into multiple climate chambers (binder) with adjustable stabilized temperature set to 25 °C for all experiments reported here. All channels are controlled by an open-source software stack, described previously.[27] Briefly, cycling instructions are handed over by the tomato app[33] to the cyclers, and the output data from the cyclers is parsed by the yagd app.[34,35] Due to a notorious lack of channels, we recently added another 1280 battery cycling channels to this infrastructure (Neware WHW 200 L), which will be interfaced with tomato and yadg. Design of experiment and data analysis was carried out in the Aurora cycler manager app[36] (or the AiiDAlab Aurora app).[37] External requests to the Aurora platform will be managed through the workflow management software AiiDA,[38] guaranteeing comprehensive data provenance tracking (not yet fully implemented).

To advance the principles of findable, accessible, interoperable, and reusable (FAIR) data, we are in the process of implementing semantic annotations into the Aurora data structure following the BattINFO ontology.[39,40] Metadata describing the cell assembly and cycling protocols is encoded in a semantically fully annotated, human-readable, BattINFO-compliant, linked-data .json format. Cell cycling data is reported as time series data in the battery data format (bdf) proposed by the Linux Foundation Energy Battery Data Alliance[41] in both plain-text, comma-separated .csv and binary, and tabular .parquet format. All cell cycling data reported here, along with the corresponding cell assembly and cycling protocol metadata, is publicly available via the open research data repository Zenodo.[42]

To promote and facilitate broad adoption of semantic annotations across the battery materials research community, we developed a metadata schema for coin cells in .xlsx format that can be converted into a BattINFO-compliant .json format with the open-source app BattINFO converter,[43] which is also provided as a web-based app,[44] not requiring any local installation. The philosophy behind the BattINFO converter app is described in ref. [45] of this Battery2030+ special issue. The advantages of semantically annotated linked data are discussed in detail in ref. [46] of this Battery2030+ special issue.

Coin cells were assembled with commercial R2032 coin cell parts (Hohsen), glass fiber separators (Whatman GF/D), graphite electrodes with a nominal areal capacity of 1.2 mAh cm^{-2} (CustomCells), LiNis$_{0.60}$Mn$_{0.20}$Co$_{0.20}$O$_2$ (NMC622), LiNi$_{0.83}$Mn$_{0.10}$Co$_{0.07}$O$_2$ (NMC811), or LiFePO$_4$ (LFP) electrodes with a nominal areal capacity of 1.0 mAh cm^{-2} (CustomCells), battery-grade ethylene carbonate (EC) and ethyl methyl carbonate (EMC) electrolyte solvent (Solvionic), LiPF$_6$ electrolyte salt (Solvionic) and fluorethylene carbonate (FEC) electrolyte additive (E-Lyte). Graphite electrodes, NMC, and LFP electrodes, and separators were punched into discs with diameters of 15, 14, and 16 mm, respectively, using dedicated

punching tools (El-Cell). Recent improvements in component handling also allow the use of the more delicate polypropylene separators (e.g., Celgard 2500) instead of the more robust glass fiber separators. All cells reported hereafter were assembled and crimped automatically by the robot in the sequence stainless steel cell can (Figure 1b), negative electrode (Figure 1e), separator (Figure 1f), 100 μl electrolyte (Figure 1g), positive electrode (Figure 1h), 1 mm stainless steel spacer, stainless steel spring, and stainless steel cell lid. The crimping force on the crimping station (Figure 1i) was 6.2 kN.

For the experiments described in **Figure 4** and **5**, NMC622 and graphite electrodes with different mass loadings were fabricated by tape casting. The slurry for NMC622 was prepared by dissolving 30.0 mg of polyvinylidene difluoride (PVDF, MTI) per ml of N-methyl-2-pyrrolidine (NMP, Sigma-Aldrich) and adding NMC622 (Gelon) and carbon black (C65, Imerys) at a NMC622:carbon black:PVDF weight ratio of 96:2:2 followed by mixing at 2000 rpm for 20 min followed by 500 rpm for 5 min (Thinky Slurry Mixer 250). The slurry for graphite electrodes was prepared by dissolving 37.2 mg of carboxymethyl cellulose (CMC, Sigma-Aldrich) and 14.0 mg of styrene-butadiene rubber (SBR, MTI) per ml of deionized water and adding graphite (Gelon) at a graphite:CMC:SBR weight ratio of 96.5:2:1.5. The mixture was stirred for 3 h and then transferred to the mixer applying the same mixing protocol. The NMC622 and graphite slurry was tape cast on aluminum and copper foil, respectively, then dried at 80 °C for 2 h, punched into 14 and 15 mm diameter discs, respectively, and calendered at 1 t cm^{-2} for 30 min, before drying at 120 and 100 °C, respectively, for 12 h in vacuum (Büchi B585) and then transferred into the argon-filled glovebox.

Nuclear magnetic resonance spectroscopy (Bruker AV III HD 400 MHz) was employed to independently confirm the EC:EMC ratio of the electrolytes mixed by the robot. Electrolyte density was determined using a densimeter (Anton Paar DMA 4100).

3. Results and Discussion

Figure 2 shows experimental data of an NMC622||graphite cell with 1M LiPF$_6$ in EC:EMC, 3:7 by volume, and 2 mol% FEC assembled by the robot. Figure 2a specifies the cycling protocol, which consists of three formation cycles at an applied current density of 0.1 mA cm^{-2} followed by long-term cycling at 1.0 mA cm^{-2} (corresponding to nominal dis-/charge rates of C/10 and 1C, i.e., with respect to the areal capacity declared by the manufacturer). The current provided here is normalized by the NMC622 electrode area. Initially at open circuit, the cell was charged to an upper cut-off voltage of 4.2 V and then discharged and charged repeatedly between a lower and upper cut-off voltage of 2.5 and 4.2 V as shown in Figure 2b. Every time the cell reaches the upper cut-off voltage of 4.2 V, the voltage is held constant until the current drops to 0.05 mA cm^{-2} (nominally C/20). Note that the nominal areal capacities may vary slightly from electrode to electrode and depend on the upper cut-off voltage and current density that was employed to measure them, the exact configuration of the cell, the degree of aging, etc.

This becomes apparent in Figure 2c, which presents voltage versus capacity curves during charge and discharge for every
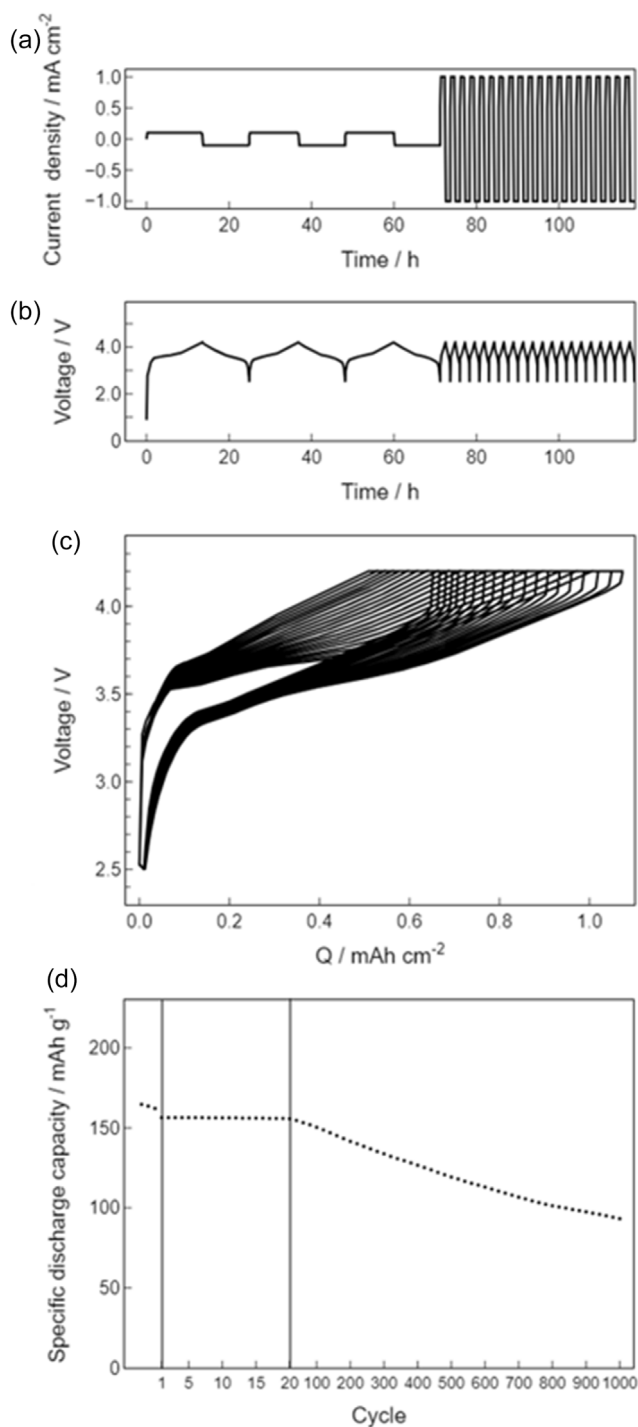
Batteries & Supercaps

Research Article
doi.org/10.1002/batt.202500155

Chemistry
Europe

European Chemical
Societies Publishing

Figure 2. Electrochemical characterization of a NMC622||graphite cell assembled by the Aurora robot: a) current density versus time, b) cell voltage versus time, c) cell voltage versus capacity for every 50th cycle at 1.0 mA cm^{-2} up to 1000 cycles, and d) specific discharge capacity versus cycle number.

mass of the NMC622 active material determined by the robot (after subtraction of the mass of the current collector, the mass of the binder, and the mass of the conductive carbon additives, as specified by the electrode manufacturer). In this representation, the discharge capacity for the three formation cycles at 0.1 mA cm^{-2} is plotted first, followed by the discharge capacity for the 1000 cycles at 1.0 mA cm^{-2}. Note that we plot the discharge capacity for each cycle during the first 20 cycles, but then only for every 20th cycle from cycle 20 onward. This approach of presenting the data provides a detailed view of the early cycling behavior while also offering a concise yet informative overview of long-term cycling performance. The capacity retention at cycle 1000 with respect to cycle 1 is 60%.

An immediate question that follows is, how reproducible are the results in Figure 2. The NMC622||graphite cell in Figure 2 was assembled along with 35 additional cells in the same batch. Two of these cells did not show an appreciable open-circuit voltage and were not cycled. The distribution of specific discharge capacities for the 34 functional cells is plotted as a histogram in **Figure 3**a. Assuming a symmetric Gaussian distribution, the mean discharge capacity is 160.7 mAh g^{-1} with a standard deviation of 2.3 mAh g^{-1} or 1.4%. We can compare these values with values for 36 NMC811||graphite cells shown in Figure 3b, with a mean discharge capacity of 198.2 mAh g^{-1} and a standard deviation of only 1.4 mAh g^{-1} or 0.7%.

Although comparable at first sight, the NMC622 and NMC811 electrodes behave very differently when punched, leading to pronounced warping of the resulting discs in the case of NMC622 electrodes, while the NMC811 electrodes stay flat. Non-planar electrodes are more challenging to assemble into coin cells than planar electrodes, possibly explaining the improvement in standard deviation. While warped electrode discs can be treated, e.g., by thermal annealing under a weight, it should be noted that such a flattening treatment can introduce cracks and other defects into the electrode, which in turn can result in a higher standard deviation.

A quantitative assessment of the misalignment of the different cell components from the video recordings of the assembly process confirms that the NMC622 electrodes tend to exhibit a slightly larger mean misalignment of 0.8–0.9 mm versus only 0.6–0.7 mm for the NMC811 electrodes, and for comparison 0.4–0.5 mm for the graphite electrodes and for the separators. We also conducted an experiment in which we misaligned NMC622 electrodes intentionally by 0.5 mm. Interestingly, the cell cycling results (not shown here) show no correlation with the intentional misalignment indicating that the choice of an oversized 15 mm diameter negative electrode in combination with a 14 mm diameter positive electrode results in very robust results with respect to their mutual misalignment (provided the overlap is maintained, see ref. [47]). We thus suspect that the increased standard deviation of the specific discharge capacities for the cells with the warped positive electrodes in Figure 3a is mainly caused by defects in the electrodes induced, e.g., by the flattening of the electrodes.

The beauty of an experiment with a batch of cells is that statistical analysis can be employed, e.g., during the formation cycles, to qualify cells in a batch for subsequent experiments.
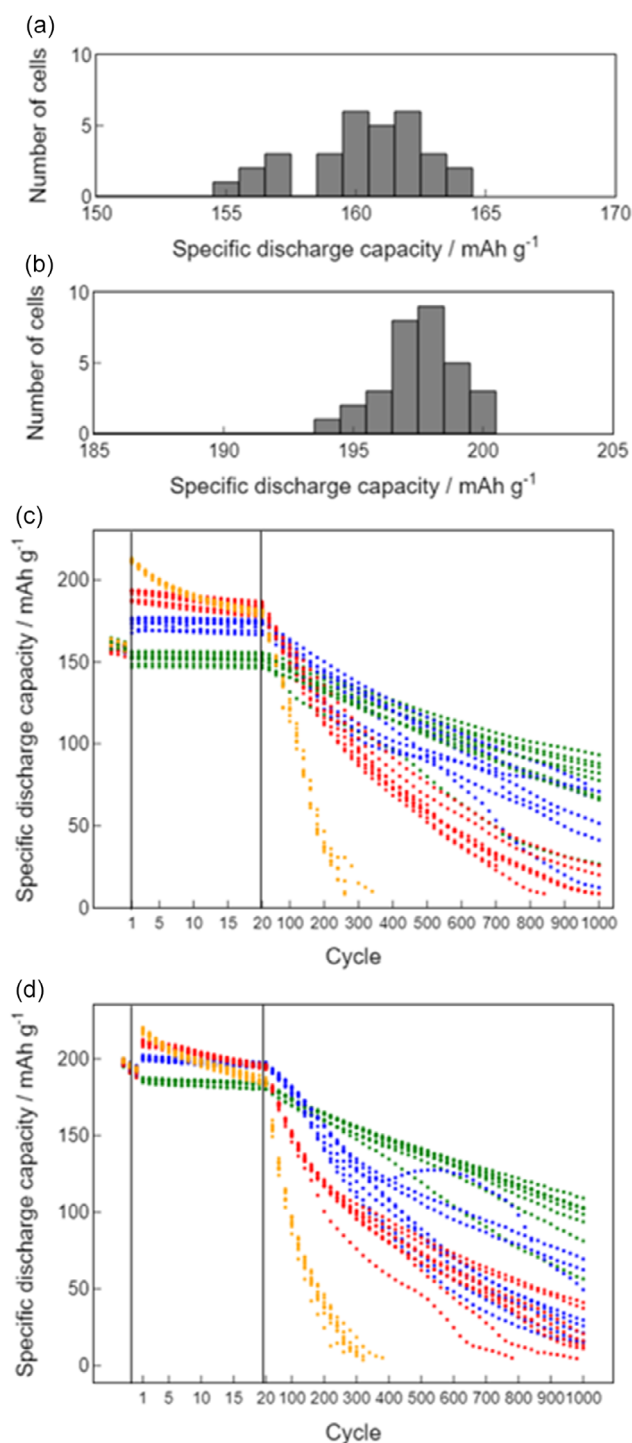
50th cycle at 1.0 mA cm^{-2} up to cycle 1000. During the first 100 cycles, the cell delivers an areal capacity slightly above 1.0 mAh cm^{-2} which then drops below 1.0 mAh cm^{-2} due to capacity fading.

The specific discharge capacity as a function of cycle number is shown in Figure 2d. The capacity here is normalized by the

Figure 3. Distribution of specific discharge capacities of a) NMC622‖graphite cells and b) NMC811‖graphite cells after the first formation cycle at 0.1 mA cm^{-2} to an upper cut-off voltage of 4.2 V. Specific discharge capacities versus cycle number of c) NMC622‖graphite cells and d) NMC811‖graphite cells cycled to an upper cut-off voltage of 4.2 V (green), 4.4 V (blue), 4.6 V (red), and 4.8 V (yellow).

Figure 4. Distribution of areal capacity of a) NMC622 and b) graphite electrodes, c) corresponding distribution of $n{:}p$ ratios selected by the Aurora robot, and d) specific discharge capacities versus cycle number for the corresponding cells. Data points in (d) are colored according to the corresponding cell's $n{:}p$ ratio in (c).

After qualification, qualified cells can in principle be divided into sub-batches, which are undergoing differing experimental conditions. This is illustrated in Figure 3c,d, where the cells are cycled in sub-batches of 8+ cells to upper cut-off voltages of 4.2, 4.4, 4.6, and 4.8 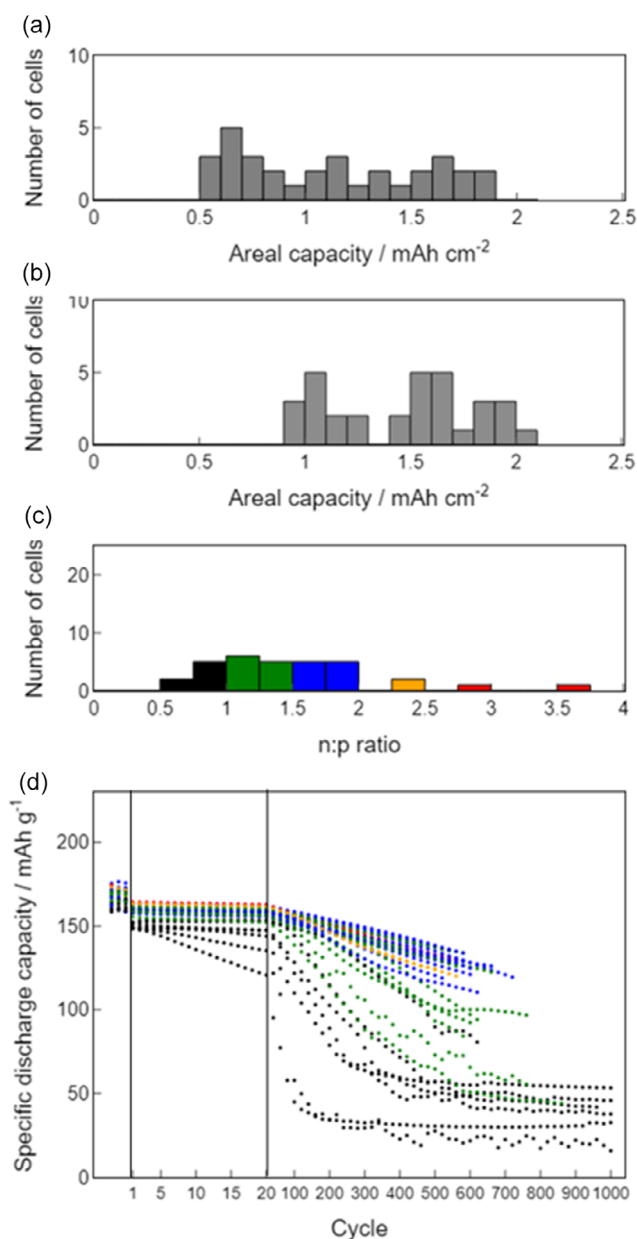V after qualification during formation cycling to an upper cut-off voltage of 4.2 V. During the first 20 cycles and beyond, the cells maintain a narrow standard deviation. As the cells approach their 1000th cycle, they do diverge steadily, including also a few cells with a more peculiar behavior. Such outliers are not unexpected, taking into account that cells are subject to many different potential aging mechanisms. We anticipate that advanced data science methods in conjunction with such carefully curated data sets will help to improve our understanding of battery aging in the coming years.

An interesting application for batches of automatically assembled cells is the study of electrode balancing. While electrodes manufactured on industrial pilot or production lines (ideally)
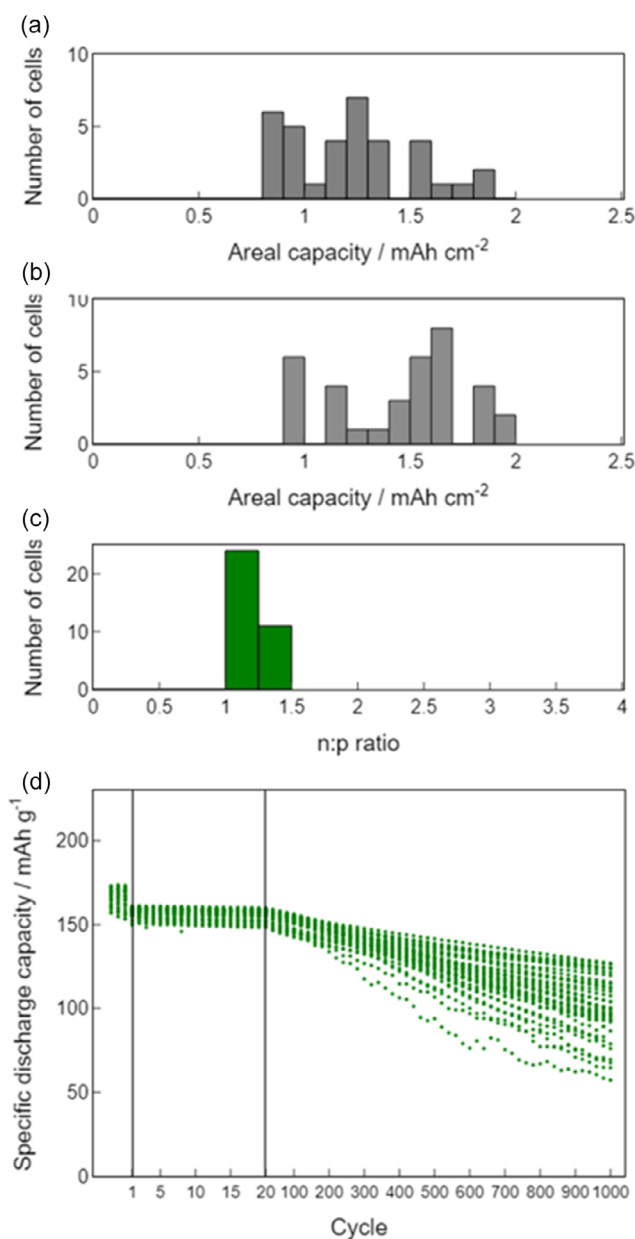
Figure 5. Distribution of areal capacity of a) NMC622 and b) graphite electrodes, c) corresponding distribution of n:p ratios selected by the Aurora robot, and d) specific discharge capacities versus cycle number for the corresponding cells.

exhibit a narrow distribution in terms of mass loading and areal capacity, electrodes manufactured manually, e.g., by tape casting in research labs, often show larger deviations in uniformity. However, such manually coated electrodes remain very important for battery materials research, as they can be fabricated already with as little as a fraction of 1 g of active material, while pilot lines typically require much larger quantities.

Figure 4a,b shows the distribution of areal capacity values for manually coated NMC622 positive electrodes and graphite negative electrodes determined by the robot. In this experiment, we have attempted to capture a large spread of values for the sake of demonstration, while with a bit of care during tape casting, the spread can be reduced significantly also for manually

coated electrodes. The large spread in areal electrode capacities allows us to design an experiment with the intention to explore the impact of a wide range of n:p ratios shown in Figure 4c on cell stability. Within the range of available electrodes, the robot allocates these pairs automatically. Figure 4d shows the outcome of this experiment (not all cells completed 1000 cycles due to a power outage). The colors of the data points match the colors in the histogram in Figure 4c. Black data points correspond to cells with $n:p < 1$, which are prone to lithium plating and thus tend to fail rapidly. Yellow and red data points correspond to cells with $n:p > 2.0$ and are thus in principle subject to more pronounced solid electrolyte interphase formation on the graphite electrode although more data is required to confirm this trend. In this experiment, the dis-/charge current density was adjusted individually for each cell according to the mass loading of the NMC622 electrode derived from the weight of the electrode determined by the robot in order to maintain a dis-/charge rate of C/10 during the formation cycling and 1C during long-term cycling. Note that the discharge capacity during the initial 20 cycles in Figure 4d is roughly scaling with the n:p ratio, i.e., lower n:p ratio yields lower discharge capacity. This can be explained by more pronounced ion transport limitations in the pores of the thicker positive electrodes employed to obtain lower n:p ratio.

Alternatively, we can design an experiment in which we request the robot to match pairs of positive and negative electrodes in such a way that the resulting n:p ratios are as close as possible to the target n:p ratio of 1.2. Results are shown in Figure 5. Figure 5d shows the outcome of the experiment investigating the cell performance at (nearly) constant n:p ratio, showing a much narrower distribution of the discharge capacities than in Figure 4d.

Figure 6 focuses on the electrolyte formulation capabilities of the Aurora robot. In Figure 6a, we analyze electrolyte solvent mixtures with different EC:EMC ratios prepared by the Aurora robot and confirm the solvent ratios independently by nuclear magnetic resonance spectroscopy. Initial mixing experiments (open symbols) were compromised by the formation of bubbles in the electrolyte dispensing tip, possibly due to crystallized electrolyte salt residues. Bubbles can be avoided using fresh tips or by thorough prior rinsing of the dispensing tips (two times for 20 s at 30 mL min^{-1} with dimethyl carbonate), resulting in an excellent 1:1 correspondence between the solvent ratios requested from the robot and the solvent ratios detected by nuclear magnetic resonance (filled symbols). A linear fit to this data set yields a slope of 0.99 ± 0.04 and an intercept of 0.02 ± 0.03, resulting in a very small error on the electrolyte solvent ratio. To avoid cross-contamination between different electrolyte formulations, single-use dispensing tips can be employed.

In Figure 6b,c, we compare the electrochemical performance of NMC622||graphite cells with different LiPF$_6$ concentrations (0.5, 1, and 1.5 M) and different EC:EMC ratios (3:7 and 7:3). After three formation cycles at 0.1 mA cm^{-2}, cells were subjected to a rate test consisting of ten cycles each at 0.33, 1.0, and 2.0 mA cm^{-2}, followed by long-term cycling at 0.33 mA cm^{-2}. The cells were cycled to an upper cut-off voltage of 4.2 V. As can be seen from the comparison of Figure 6b,c, the cells with 0.5M LiPF$_6$ (green) show the
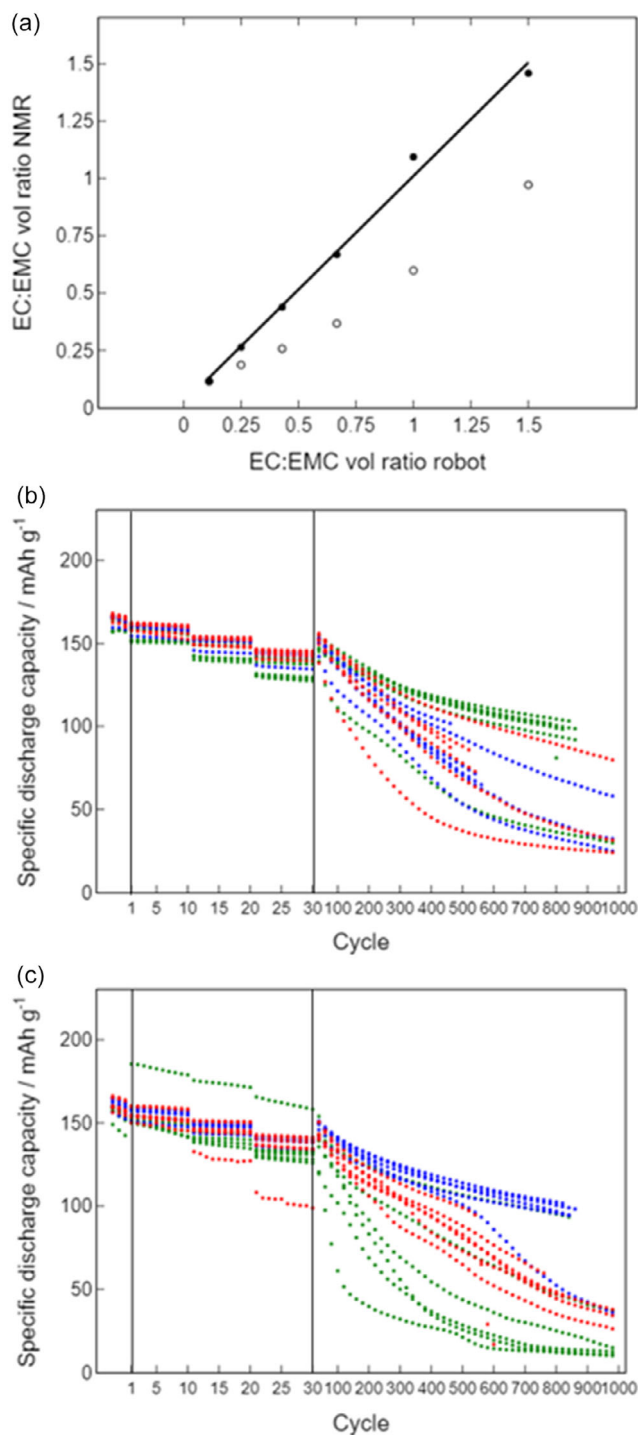
Batteries & Supercaps

Research Article
doi.org/10.1002/batt.202500155

Chemistry Europe
European Chemical
Societies Publishing

more viscous electrolyte with EC:EMC ratio of 7:3. This observation can be at least partially rationalized by invoking the tendency of $LiPF_6$ to decompose and liberate fluorine ions during cycling.[48,49] A low $LiPF_6$ salt concentration thus possibly improves the long-term cycling stability by liberating fewer fluorine ions, while the electrolyte with high viscosity reduces the mobility of lithium
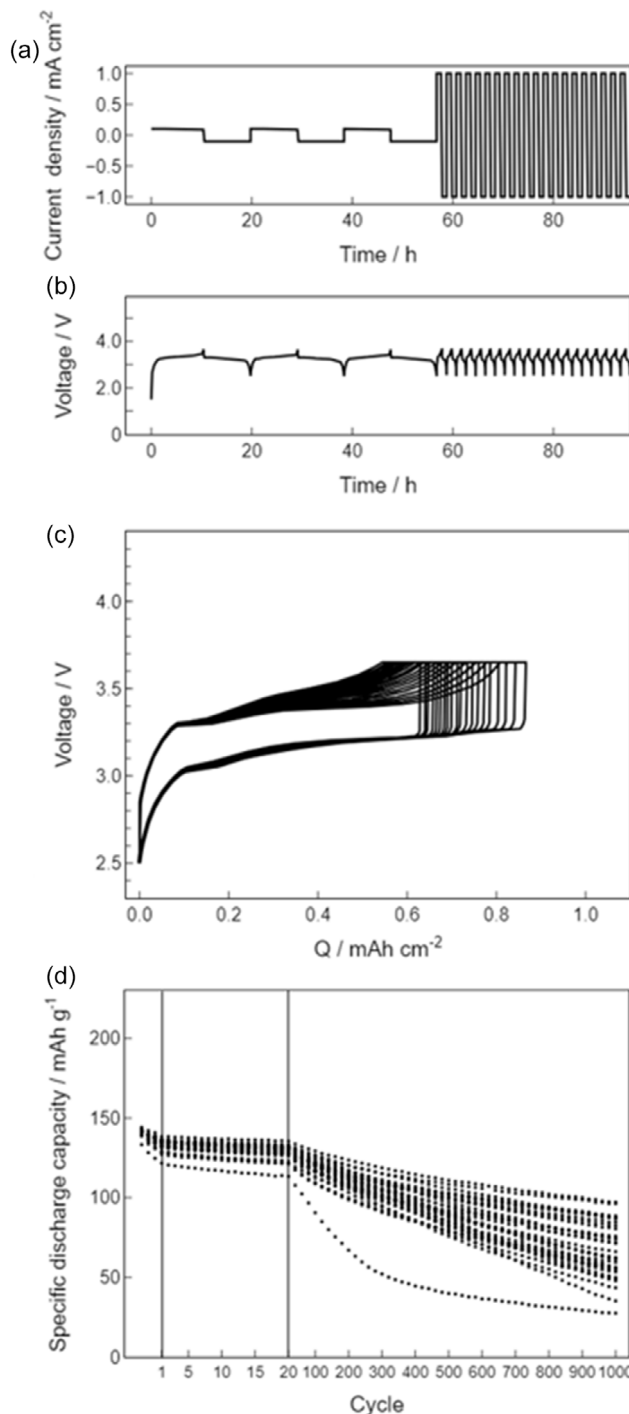

Figure 6. a) EC:EMC electrolyte solvent ratio confirmed by nuclear magnetic resonance versus solvent ratio set by the robot. Specific discharge capacity versus cycle number for NMC622∥graphite cells with 0.5 M (green), 1.0 M (blue), and 1.5 M (red) $LiPF_6$ in b) EC:EMC = 3:7 and c) EC:EMC = 7:3.

poorest rate performance for both EC:EMC ratios due to the low lithium-ion conductivity at this low salt concentration.

Interestingly, the cells with 0.5 M $LiPF_6$ concentration (green) and an EC:EMC ratio of 3:7 in Figure 6c perform best in terms of capacity retention during long-term cycling, while the cells with intermediate 1.0 M $LiPF_6$ concentration (blue) perform best in the

Figure 7. Electrochemical characterization of a LFP∥graphite cell assembled by the Aurora robot: a) current density versus time, b) cell voltage versus time, c) cell voltage versus capacity for every 50th cycle at 1.0 mA cm^{-2} up to 1000 cycles, and d) specific discharge capacity versus cycle number for all 36 cells in this batch.

Batteries & Supercaps

Research Article
doi.org/10.1002/batt.202500155

Chemistry Europe
European Chemical
Societies Publishing

and fluorine ions in the electrolyte, favoring the intermediate $LiPF_6$ salt concentration. A more detailed study would be necessary to fully understand the implications of changing salt concentration and electrolyte solvent ratio. However, the data presented in Figure 6c clearly demonstrates the power of using automation to obtain statistically relevant results. Although automated experiments are not immune to outliers (see, e.g., Figure 6c), which may have a cause not related to the assembly process, such as a defect in the electrode from the electrode coating process, they nevertheless provide the statistics to identify these outliers.

Finally, recognizing the value of well-curated, richly annotated datasets that adhere to FAIR data principles and reporting standards for modeling and machine learning studies including transfer learning approaches, we provide all cell cycling data and corresponding metadata publicly via the Zenodo repository.[42] We also include a data set of a batch of 36 LFP‖graphite cells with 1 M $LiPF_6$ in EC:EMC, 3:7 by volume, and 2 mol% FEC cycled to an upper cut-off voltage of 3.65 V with a mean discharge capacity of 164.8 mAh g^{-1} and a standard deviation of 3.6 mAh g^{-1} shown in **Figure 7**. The best cell shows a capacity retention of 70% at cycle 1000 with respect to cycle 1.

4. Conclusions and Outlook

Presenting a number of research cases and validation studies using the example of the benchmark NMC‖graphite and LFP‖graphite battery chemistries with carbonate-based electrolytes, we illustrated and demonstrated the current capabilities and features of our automated robotic battery materials research platform, Aurora. While further hardware and software developments are ongoing, Aurora is now operational to address real-world research questions.

Our development roadmap for the Aurora platform foresees an even tighter integration with the open-source workflow management software AiiDA,[38,50,51] which will be the central hub for handling requests to the Aurora platform and guarantees data provenance tracking. Requests may not only include the specification of electrode composition, electrolyte formulation, cell assembly instructions, and cycling protocols, but also dynamic requests for the exchange of data between the Aurora platform and its data repository and the exchange of data between the data repository and external users. We are currently implementing data transfer protocols between the Aurora platform and the open-source data management platform openBIS[52,53] developed by ETH Zurich, which will serve as Aurora's central data repository. While we are coupling the Aurora robot platform with the AiiDA workflow management platform and the openBIS data management platform, we prioritize interoperability and platform agnosticism by structuring the data within the BattINFO ontology[39,40] framework and reporting cycling data in battery data format.[41] This approach ensures seamless integration and exchange of data across different platforms.

Workflow and data management automation also facilitates the interaction with external modeling and machine learning agents receiving data from the Aurora platform and sending back instructions for subsequent experiments, thereby increasing step-by-step the autonomy of the Aurora platform.

Ultimately, one could consider offering the capabilities of Aurora and other robotic platforms with a high degree of automation as research as a service in analogy to, e.g., synchrotron facilities. The development of such a facility focusing on the development of novel catalysts is currently ongoing at ETH Zurich and EPFL[54,55] and could be implemented analogously for battery research with the availability of the required funding. With the commercial availability of the Aurora platform and other commercial robotic platforms and the availability of various open-source software packages including an open-source package to control the Aurora platform,[56,57] such a facility could also operate in a decentralized, cloud-connected, and orchestrated manner realizing the vision of a community-driven, seamlessly interconnected, autonomous cloud lab that accelerates battery materials research.

Conflict of Interest

The authors declare no conflict of interest.

Data Availability Statement

The data that support the findings of this study are openly available in Zenodo at https://doi.org/10.5281/zenodo.15481956, reference number 15481956.

Batteries & Supercaps

Research Article
doi.org/10.1002/batt.202500155

Chemistry Europe
European Chemical
Societies Publishing

[1] C. Tan, H. Wu, L. Yang, Z. Wang, *Adv. Mater. Technol.* **2024**, *9*, 2302038.

[2] J.-P. Correa-Baena, K. Hippalgaonkar, J. van Duren, S. Jaffer, V. R. Chandrasekhar, V. Stevanovic, C. Wadia, S. Guha, T. Buonassisi, *Joule* **2018**, *2*, 1410.

[3] S. P. Stier, C. Kreisbeck, H. Ihssen, M. A. Popp, J. Hauch, K. Malek, M. Reynaud, T. P. M. Goumans, J. Carlsson, I. Todorov, L. Gold, A. Räder, W. Wenzel, S. T. Bandesha, P. Jacques, F. Garcia-Moreno, O. Arcelus, P. Friederich, S. Clark, M. Maglione, A. Laukkanen, I. E. Castelli, J. Carrasco, M. C. Cabanas, H. S. Stein, O. Ozcan, D. Elbert, K. Reuter, C. Scheurer, M. Demura, et al., *Adv. Mater.* **2024**, *36*, 2407791.

[4] E. O. Pyzer-Knapp, J. W. Pitera, P. W. J. Staar, S. Takeda, T. Laino, D. P. Sanders, J. Sexton, J. R. Smith, A. Curioni, *npj Comput. Mater.* **2022**, *8*, 84.

[5] G. Scheider, *Nat. Rev. Drug Discovery* **2018**, *17*, 97.

[6] D. Tabor, L. M. Roch, S. K. Saikin, C. Kreisbeck, D. Sheberla, J. H. Montoya, S. Dwaraknath, M. Aykol, C. Ortiz, H. Tribukait, C. Amador-Bedolla, C. J. Brabec, B. Maruyama, K. A. Persson, A. Aspuru-Guzik, *Nat. Rev. Mater.* **2018**, *3*, 5.

[7] A. Senocrate, F. Bernasconi, P. Kraus, N. Plainpan, J. Trafkowski, F. Tolle, T. Weber, U. Sauter, C. Battaglia, *Nat. Catal.* **2024**, *7*, 742.

[8] J. Amici, P. Asinari, E. Ayerbe, P. Barboux, P. Bayle-Guillemaud, R. J. Behm, M. Berecibar, E. Berg, A. Bhowmik, S. Bodoardo, I. E. Castelli, I. Cekic-Laskovic, R. Christensen, S. Clark, R. Diehm, R. Dominko, M. Fichtner, A. A. Franco, N. Guillet, M. Hahlin, S. Hartmann, V. Heiries, K. Hermansson, A. Heuer, S. Jana, L. Jabbour, J. Kallo, A. Latz, H. Lorrmann, et al., *Adv. Energy Mater.* **2022**, *12*, 2102785.

[9] J.-M. Tarascon, *Nat. Mater.* **2022**, *21*, 979.

[10] M. R. Palacin, *Acc. Mater. Res.* **2021**, *2*, 319.

[11] V. Pellegrini, S. Bodoardo, D. Brandell, K. Edström, *Solid State Commun.* **2019**, *303–304*, 113733.

[12] M. T. McDowell, *Nano Lett.* **2021**, *21*, 6353.

[13] E. McCalla, *ACS Eng. Au* **2023**, *3*, 391.

[14] A. Dave, J. Mitchell, K. Kandasamy, H. Wang, S. Burke, B. Paria, B. Póczos, J. Whitacre, V. Viswanathan, *Cell Rep. Phys. Sci.* **2020**, *1*, 100264.

[15] A. Dave, J. Mitchell, S. Burke, H. Lin, J. Whitacre, V. Viswanathan, *Nat. Commun.* **2022**, *13*, 5454.

[16] S. Matsuda, K. Nishioka, S. Nakanishi, *Sci. Rep.* **2019**, *9*, 6211.

[17] P. H. Svensson, P. Yushmanov, A. Tot, L. Kloo, E. Berg, K. Edström, *Chem. Eng. J.* **2023**, *455*, 140955.

[18] A. Benayad, D. Diddens, A. Heuer, A. N. Krishnamoorthy, M. Maiti, F. L. Cras, M. Legallais, F. Rahmanian, Y. Shin, H. Stein, M. Winter, C. Wölke, P. Yan, I. Cekic-Laskovic, *Adv. Energy Mater.* **2022**, *12*, 2102678.

[19] T. Adhikari, A. Hebert, M. Adamič, J. Yao, K. Potts, E. McCalla, *ACS Comb. Sci.* **2020**, *22*, 311.

[20] M. S. Beal, B. E. Hayden, T. L. Gall, C. E. Lee, X. Lu, M. Mirsaneh, C. Mormiche, D. Pasero, D. C. A. Smith, A. Weld, C. Yada, S. Yokoishi, *ACS Comb. Sci.* **2011**, *13*, 375.

[21] B. Aoun, C. Yu, L. Fan, Z. Chen, K. Amine, Y. Ren, *J. Power Sources* **2015**, *279*, 246.

[22] P. Liu, B. Guo, T. An, H. Fang, G. Zhu, C. Jiang, X. Jiang, *J. Materiomics* **2017**, *3*, 202.

[23] M. Vogler, S. K. Steensen, F. F. Ramrez, L. Merker, J. Busk, J. M. Carlsson, L. H. Rieger, B. Zhang, F. Liot, G. Pizzi, F. Hanke, E. Flores, H. Hajiyani, S. Fuchs, A. Sanin, M. Gaberšček, I. E. Castelli, S. Clark, T. Vegge, A. Bhowmik, H. S. Stein, *Adv. Energy Mater.* **2024**, *14*, 2403263.

[24] F. Rahmanian, S. Fuchs, B. Zhang, M. Fichtner, H. S. Stein, *Digital Discovery* **2024**, *3*, 883.

[25] B. Zhang, L. Merker, A. Sanin, H. S. Stein, *Digital Discovery* **2022**, *1*, 755.

[26] J. T. Yik, L. Zhang, J. Sjölund, X. Hou, P. H. Svensson, K. Edström, E. J. Berg, *Digital Discovery* **2023**, *2*, 799.

[27] P. Kraus, E. Bainglass, F. F. Ramirez, E. Svaluto-Ferro, L. Ercole, B. Kunz, S. P. Huber, N. Plainpan, N. Marzari, C. Battaglia, G. Pizzi, *J. Mater. Chem. A* **2024**, *12*, 10773.

[28] V. Murray, D. S. Hall, J. R. Dahn, *J. Electrochem. Soc.* **2019**, *166*, A329.

[29] A. U. Schmid, M. Kurka, K. P. Birke, *J. Energy Storage* **2019**, *24*, 100732.

[30] B. R. Long, S. G. Rinaldo, K. G. Gallagher, D. W. Dees, S. E. Trask, B. J. Polzin, A. N. Jansen, D. P. Abraham, I. Bloom, J. Bareño, J. R. Croy, *J. Electrochem. Soc.* **2016**, *163*, A2999.

[31] M. G. Nam, H. J. Song, J. K. Koo, G. H. Choi, Y. S. Kim, H. J. Kim, C.-S. Shin, Y. Kim, J. H. Nah, Y.-J. Kim, P. J. Yoo, *Commun. Mater.* **2024**, *5*, 29.

[32] F. Dai, M. Cai, *Commun. Mater.* **2022**, *3*, 64.

[33] https://github.com/EmpaEconversion/tomato (accessed: February 2025).

[34] P. Kraus, N. Vetsch, C. Battaglia, *J. Open Source Software* **2022**, *7*, 4166.

[35] https://github.com/EmpaEconversion/yadg (accessed: February 2025).

[36] https://github.com/EmpaEconversion/aurora-cycler-manager (accessed: February 2025).

[37] https://github.com/EmpaEconversion/aiidalab-aurora (accessed: February 2025).

[38] S. P. Huber, S. Zoupanos, M. Uhrin, L. Talirz, L. Kahle, R. Häuselmann, D. Gresch, T. Müller, A. V. Yakutovich, C. W. Andersen, F. F. Ramirez, C. S. Adorf, F. Gargiulo, S. Kumbhar, E. Passaro, C. Johnston, A. Merkys, A. Cepellotti, N. Mounet, N. Marzari, *Sci. Data* **2020**, *7*, 300.

[39] S. Clark, F. L. Bleken, S. Stier, E. Flores, C. W. Andersen, M. Marcinek, A. Szczesna-Chrzan, M. Gaberscek, M. R. Palacin, M. Uhrin, J. Friis, *Adv. Energy Mater.* **2022**, *12*, 2102702.

[40] https://big-map.github.io/BattINFO/index.html (accessed: February 2025).

[41] https://github.com/battery-data-alliance/battery-data-format (accessed: February 2025).

[42] https://doi.org/10.5281/zenodo.15481956.

[43] https://github.com/EmpaEconversion/BattINFOConverter (accessed: February 2025).

[44] https://BattINFOConverter.streamlit.app/ (accessed: February 2025).

[45] N. Plainpan, S. Clark, C. Battaglia, *Batteries & Supercaps*, **2025**, https://doi.org/10.1002/batt.202500151.

[46] S. Clark, C. Battaglia, I. E. Castelli, E. Flores, L. Gold, C. Punckt, S. Stier, P. Veit, *ChemSusChem* **2025**, https://doi.org/10.1002/cssc.202500458.

[47] N. Kim, Y. Byun, D. Jin, C. B. Dzakpasu, S. H. Park, H. Lee, S.-T. Hong, Y. M. Lee, *J. Electrochem. Soc.* **2022**, *169*, 023502.

[48] K. Xu, *Chem. Rev.* **2004**, *104*, 4303.

[49] C. Bolli, A. Guéguen, M. A. Mendez, E. J. Berg, *Chem. Mater.* **2019**, *31*, 1258.

[50] https://www.aiida.net/ (accessed: February 2025).

[51] https://github.com/aiidateam/aiida-core (accessed: February 2025).

[52] https://openbis.ch/ (accessed: February 2025).

[53] https://sissource.ethz.ch/sispub/openbis (accessed: February 2025).

[54] P. Laveille, P. Miéville, S. Chatterjee, E. Clerc, J.-C. Cousty, F. Nanteuil, E. Lama, E. Mariano, A. Ramirez, U. Randrianarisoa, K. Villat, C. Copéret, N. Cramer, *CHIMIA* **2023**, *77*, 154.

[55] https://swisscatplus.ch/ (accessed: February 2025).

[56] M. Seifrid, F. Strieth-Kalthoff, M. Haddadnia, T. C. Wu, E. Alca, L. Bodo, S. Arellano-Rubach, N. Yoshikawa, M. Skreta, R. Keunen, A. Aspuru-Guzik, *Digital Discovery* **2024**, *3*, 1319.

[57] https://aspuru-guzik-group.gitlab.io/self-driving-lab/instruments/chemspyd/ (accessed: February 2025).